# Microwave sintering of zirconia toughened alumina - Influence of the type and content of doping in zirconia

Nouhaila Khalile, Clémence Petit, Christophe Meunier, François Valdivieso

HAL Id: emse-04191173

https://hal-emse.ccsd.cnrs.fr/emse-04191173

Submitted on 30 Aug 2023

# Microwave sintering of Zirconia Toughened Alumina - Influence of the type and content of doping in zirconia

Nouhaila Khalile, Clémence Petit*, Christophe Meunier, François Valdivieso

Mines Saint-Etienne, Univ Lyon, CNRS, UMR 5307 LGF, Centre SMS, F-42023 Saint-Etienne

France

*Corresponding author: Clémence Petit, clemence.petit@emse.fr

Mines Saint-Etienne, Univ Lyon, CNRS, UMR 5307 LGF, Centre SMS, F-42023 Saint-Etienne

France

**Abstract**

This study focuses on the influence of zirconia on microwave (MW) sintering of zirconia-toughened alumina (ZTA). ZTA samples containing various zirconia powders (unstabilized and stabilized with yttria or ceria) were sintered in a MW cavity, in a sintering cell with or without susceptor. 8 mol% yttria-stabilized zirconia was denser when it was sintered without susceptor. The densification curves also showed different behaviours in the intermediate stage of sintering, between the four samples. The samples with 3 and 8 mol% yttria-stabilized zirconia were easier to densify than the samples with unstabilized and 10 mol% ceria-stabilized zirconia samples. This was confirmed when the samples were heated in a single-mode cavity. These differences of behaviour under MW can be linked to the chemical composition of zirconia. The substitution of zirconium cation by yttrium in the lattice generates an excess of oxygen vacancies and of dipoles. The latter are involved in the MW/material interactions.

**Keywords:** Zirconia Toughened Alumina, Doping, Microwave Sintering, Dielectric properties

# 1. Introduction

Zirconia-toughened alumina (ZTA) ceramic has been extensively studied due to its attractive properties, *i.e.*, high strength, high toughness, high hardness, good thermal shock resistance, low thermal conductivity [1, 2]. These properties make ZTA ceramics suitable for various applications, especially cutting tools [3] or biomedical applications (dental screws and orthopaedic implants) [4]. The dispersion of zirconia grains in the alumina matrix improves the flexural strength, and more specifically the fracture toughness [5, 6]. The high mechanical properties of zirconia are related to the well-known stress-induced phase transformation mechanism of metastable tetragonal zirconia [7]. The tetragonal structure of zirconia is stabilized at room temperature by addition of stabilizing oxides [8] as $CeO_2$ [9], $Y_2O_3$ [10], MgO [11] or CaO [12]. Moreover, ZTA is also known for its high resistance to ageing, or low-temperature degradation. This phenomenon consists in tetragonal to monoclinic phase transformation in zirconia occurring spontaneously at room temperature in presence of water [13]. It is a critical issue for the use of zirconia (especially 3 mol% yttria-stabilized zirconia, 3Y-TZP) orthopaedic implants.

Densification of ceramics is only achievable by sintering, which requires long thermal treatments at high temperature, commonly in resistive furnaces. Several rapid sintering processes have been developed as an alternative to conventional thermal treatments to decrease energy and time consumption [14, 15]. Among them, microwave (MW) sintering is based on heating of a material by the electromagnetic field. During MW heating, the dielectric material mainly couples with the electric field, absorbs its energy in its bulk and transforms it into heat [16]. The ability of a dielectric material to be heated by MW mainly depends on its dielectric properties. In particular, the dielectric loss tangent is defined as *tan α = ε''/ε'*, with *ε'* and *ε''* being the dielectric constant and the dielectric loss factor respectively [17]. The higher dielectric loss factor, the more material couples with the electromagnetic field and heats up quickly

Alumina is a low-loss dielectric material and is considered as transparent to MW radiation [18, 19]. This is why it is always sintered using an external susceptor. A susceptor is a material which strongly couples with MW and can transmit heat to the sample, mainly by radiation [20]. In the case where a susceptor is used, MW heating is called hybrid or indirect. 3Y-TZP couples better with MW than alumina. Its loss tangent sharply increases with temperature [21]. Therefore, the association of the two materials in ZTA can facilitate its heating by MW. But the dielectric properties of zirconia varies with its chemical and phase composition [22]. In particular, the stabilized phases and the dopants used for this stabilization can have an effect on the dielectric properties, and thus, on the MW/material interactions.

The studies about MW sintering of ZTA mainly focused on the possibility to achieve fully dense material with fine microstructure with short thermal cycles, in comparison with conventional sintering [23, 24, 25]. However, few authors compared the behaviour under MW of ZTA containing different zirconias. Khalid *et al.* densified two ZTA samples with yttria-stabilized zirconia with 3 and 8 mol% [26] but did not relate the results to the concentration of dopants.

This aim of this work is to compare MW sintering of different ZTA samples, prepared from different zirconia powders. Four zirconia powders were selected: an unstabilized, two stabilized with yttria (3 and 8 mol%) and one stabilized with ceria (10 mol%). On the one hand, the 3 mol% yttria-stabilized zirconia and 10 mol% ceria-stabilized zirconia contain two stabilizing cations with different valences (trivalent for yttrium and tetravalent for cerium). On the other hand, the two yttria-stabilized zirconia types contain the same stabilizing cations but with two different amounts. The samples were sintered in an instrumented multimode cavity in two configurations, *i.e.*, with and without a silicon carbide (SiC) susceptor. To complete these experiments, the same samples were heated in a MW single-mode resonant cavity in a direct configuration (no susceptor and no thermal insulator).

## 2. Experimental procedures

### 2.1. Shaping of samples

Commercial alumina (BMA-15, Baikowski International, specific surface: 15 m$^2$/g) and four zirconia powders were used as starting materials. The zirconia powders were: an unstabilized one (TZ0, Tosoh Corporation, specific surface: 14.8 m$^2$/g), 3 mol% yttria-stabilized one (TZ-3Y, Tosoh Corporation, specific surface: 15.7 m$^2$/g), 8 mol% yttria-stabilized one (TZ-8Y, Tosoh Corporation, specific surface: 13.6 m$^2$/g) and 10 mol% ceria-stabilized one (Daiichi Kigenso Kagaku Kogio Co. LTD, specific surface: 14.3 m$^2$/g). Adequate amounts of alumina and zirconia powders were mixed to prepare composites with 20 vol% of zirconia. The powders were dispersed in distilled water with 2.7 wt% (relative to weight of powder) of Darvan CN dipersant (Vanderbilt minerals, LLC). The amount was chosen according to preliminary tests (not shown here). The pH of the suspension was adjusted to 10 by addition of KOH. After addition of 2 wt% of PVA binder (Rhodoviol 4/125, Prolabo) and 1 wt% polyethylene glycol (Mw 1500, Prolabo), the suspension was homogenized by ball-milling during 15 hours using 2 mm-diameter alumina balls. Finally the suspension was spray-dried with a spray-dryer (mini spray-dryer BUCHI 190).

The spray-dried powders were shaped into disks by uniaxial pressing (12 mm diameter and 4 mm thickness) at 50 MPa and then isostatically pressed at 300 MPa.

The samples were debinded by heating at 1°C/min to 600°C with a dwell of 1 hour in air. The green bodies had a density in the range of 50 - 52 % T.D. (theoretical densities are 3.99 g/cm$^3$, 5.90 g/cm$^3$, 6.07 g/cm$^3$ and 5.75 g/cm$^3$ for alumina, cubic, tetragonal and monoclinic zirconia respectively).

The samples will be named A-0Z, A-3YZ, A-8YZ and A-10CeZ, for composites containing unstabilized, 3 mol% yttria-stabilized, 8 mol% yttria-stabilized and 10 mol% ceria-stabilized zirconia, respectively.

## 2.2. The MW setup and the sintering cell

MW sintering experiments were performed with a MW heating system designed and described by Zymełka *et al.* [27]. This heating device was equipped with a fixed frequency of 2.45 GHz~3 kW MW generator (GMP30K, SAIREM) connected with a multimode cavity of dimensions of 430 mm × 430 mm × 490 mm.

One of the main difficulties with the MW heating is the temperature measurement. Thus, in order to avoid disturbance of the electromagnetic waves in the cavity, contactless measurement of temperature using infrared pyrometers was performed. A bichromatic pyrometer (Lumasense Technology) sensitive to the wavelength between 2 and 2.5 µm, working in the 250-1800°C temperature range was used. To obtain an accurate value of temperature, it is necessary to know the ratio of apparent emissivity $k$ in the experimental conditions. Therefore, a calibration method based on the melting point of a metallic calibration material as described by Zymełka *et al.* [27] was used. In this study, palladium (having a melting point of 1550°C) was used as calibrating material. It was placed on a small hole engraved in the sample surface. When Pd starts melting, the ratio $k$ is recalculated so that the melting point of Pd is equal to the measured temperature.

Optical dilatometry was used to record the pellet's shrinkage during sintering. The protocol used in this work was previously described by Zuo *et al.* [28] and Meunier *et al.* [29]. A high-resolution CCD camera (SLC2050MTLGEC, 14-bit, 1600 9 1200, SVS-VISTEK), records pictures of the flat circular surface of the pellet during the thermal cycle. Then, the recorded images were used by a dedicated custom-made Labview software which detects the pellets' edges to measure the diameter. The program finally output the evolution of the pellet's diameter

during sintering. Then, the evolution of relative density was calculated with Eq. 1 taking into account the anisotropy shrinkage ratio $\alpha$ (Eq. 2).

$$\rho(t) = \frac{\left(1+\frac{h_f-h_0}{h_0}\right)*\left(1+\frac{D_f-D_0}{D_0}\right)^2}{\left(1+\frac{1}{\alpha}*\frac{D(t)-D_0}{D_0}\right)*\left(1+\frac{D(t)-D_0}{D_0}\right)^2} * \rho_f \qquad \text{(Eq. 1)}$$

$$\alpha = \frac{D_f-D_0}{D_0} * \frac{h_0}{h_f-h_0} \qquad \text{(Eq. 2)}$$

Where $\rho(t)$ is the instantaneous density of the sample, $\rho_f$ the final density, $h_f$ the final height, $h_0$ the initial height, $D_f$ the final diameter, $D_0$ the initial diameter and $D(t)$ the instantaneous diameter.

The thermal cycle was controlled by a specific custom-made LabVIEW software. It used a PID controller based on the temperature measured by pyrometers. The incident power delivered by the generator was continuously adjusted during the sintering cycle to match the measured temperature with the set temperature. It also recorded the data (power, temperature, images) useful to control the thermal treatment and to plot the dilatometric curves.

The green samples were positioned in a sintering cell, used as an insulating box in order to optimize samples' insulation and guarantee their homogeneous heating. This sintering cell has been designed and tested during previous studies [28]. The sintering cell used in this study was mainly made of different plates of aluminosilicate fibers (KVS 184-400, RATH®) as thermal insulator. This material was used because it meets the requirements of MW applications: transparency to MW, stability at high temperature (to 1800°C) and low thermal conductivity (0.33 W.m$^{-1}$.K$^{-1}$ at 1400°C). Inside the cell, the sample was placed on two alumina sample holders to record images of its flat surface. A SiC ring was used as susceptor to initiate samples' heating. A low-loss mullite tube (C610, AMTS) surrounded the sample. This tube was used to minimize the susceptor radiation received by the sample at high temperature.

## 2.3. Thermal treatments

MW sintering was carried out in the multimode cavity described in the subsection 2.2. The samples were sintered inside the sintering cell described in the subsection 2.2 in two configurations: with and without the SiC susceptor (noted SiC and noSiC respectively). The pyrometer was calibrated for each case, as explained in subsection 2.2. Values of 0.992 and 0.959 were measured for the ratio $k$ for the SiC and noSiC configurations respectively. These values were averages obtained with three measurements.

A unique thermal cycle was applied: a heating rate of 25°C/min to 1550°C and a dwell time of 10 min.

## 2.4. Characterization of sintered samples

Densities of sintered samples were measured by Archimedes' method with absolute ethanol as the liquid medium.

Image analysis was carried out by Scanning Electron Microscopy (Zeiss SUPRA 55VP) in backscattered electron mode, with a voltage of 15 kV. Before observation, the samples were cut, polished until mirror surface finishing and thermally etched at 1480°C during 10 min in a tubular furnace. The samples were quickly introduced in the hot zone of the furnace, which was previously heated to the etching temperature. The alumina and zirconia average grain sizes were measured with the linear intercept method described by Mendelson. A statistical correction factor of 1.56 was applied to calculate the average grain sizes [30]. At least 400 grains were analysed at different locations of the cut surfaces (in the volume and near the surface) for each sample using the ImageJ software.

An X-ray diffractometer (X'Pert Pro MPD, PANalytical), working with a Cu Kα radiation (wavelength of 1.5418 Å), voltage of 45 kV and current of 40 mA, was used with a linear detector in scanning mode to determine the phase composition of the sintered materials. A 2θ

range from 10 to 138° with a step size of 0.013° and counting time of 29 s/step was used. PANalytical HighScore software equipped with the ICDD PDF-4+ database was used for data interpretation. For the samples containing tetragonal and monoclinic zirconia, the volume fraction of monoclinic phase was determined from the integrated intensity of the tetragonal (101) peak and the monoclinic ($\bar{1}$11) and (111) peaks, using the equation proposed by Garvie et al. [31] and modified by Toraya et al. [32]:

$$V_m = \frac{1.311X_m}{1+0.311X_m} \qquad \text{(Eq 3)}$$

$$X_m = \frac{I_m(\bar{1}11)+I_m(111)}{I_m(\bar{1}11)+I_m(111)+I_t(101)} \qquad \text{(Eq. 4)}$$

with $V_m$ and $X_m$, volume fraction and weight fraction of monoclinic phase respectively.

### 2.5. Heating of samples in a single-mode MW cavity

In order to complete the study, direct heating of the samples in a SAIREM single-mode MW cavity was carried out. The single-mode setup used in this study was well described by Ghorbel et al. [33]. The first step was the determination of the conditions for obtaining resonant cavity (superposition of incident and reflected waves). Therefore, the sample was placed at a position corresponding to the maximum intensity of electric field using Vector Network Analyzer. Therefore, at first, the sample was placed at a fixed position and the cavity length was slightly adjusted by an automatic movable piston to obtain the minimum value of reflected power and the optimal resonance conditions to ensure efficient heating. For this study, all the pellets (diameter of 12 mm) were placed in the cavity without susceptor and thermal insulator, obtaining a configuration of direct MW heating. The pellets were heated with a constant forwarded power of 100 W applied during 9 min. The temperature at the surface of the pellet was measured by an IR pyrometer (Fluke® Process Instruments, 27 E3ML-F1-V-0-0) operating at a wavelength of 2.4 µm and an emissivity of 0.5.

## 3. Results

### 3.1. Densification curves and final densities

The sintered relative densities of each sample are given in Table 1. All the sintered relative densities are higher than 95%. There is a small difference (around 2 %) of relative density for A-8YZ and A-10CeZ between SiC and noSiC configurations. On the contrary, the values for A-0Z and A-3YZ for both sintering configurations are close.

Figure 1 presents the densification curves for the four samples sintered with SiC (Figure 1a) and without SiC (Figure 1b). The curves of the noSiC configuration are shifted towards higher temperatures, in comparison with the SiC configuration, for the A-0Z, A-3YZ and A-10CeZ samples. This shift is visible for the initial and intermediate stages of sintering. On the contrary, for the A-8YZ sample, the noSiC curve is shifted towards lower temperatures. To quantify these shifts, Table 2 reports the temperatures for which the relative density was 65 % (corresponding to the intermediate stage of sintering) for the four samples and the two sintering configurations. The difference between these temperatures ($\Delta T_{noSiC-SiC}$) is also indicated in this table. This difference is positive for A-0Z, A-3YZ and A-10CeZ with the highest value for A-0Z and the lowest one for A-3YZ. It is instead negative for A-8YZ.

### 3.2. Microstructure of sintered samples

Figure 2 shows two SEM images of the A-3YZ sample sintered with the SiC susceptor at two magnifications. Images of the other samples are shown in Suppl. Fig. 1. Zirconia and alumina are the bright and dark phases, respectively. Figure 2a shows residual pores, in relation with the final densities. The zirconia grains are dispersed in the alumina matrix, with few aggregates. Figure 2b and Suppl. Fig. 1 show submicronic grains for the two phases, with the zirconia grains located at the alumina grain boundaries.

9

Figure 3 shows the average grain sizes and the standard deviations measured on the images for each sample and each sintering configuration. The average values are in the range 0.59-0.87 µm for the alumina grains and 0.16-0.4 µm for the zirconia grains. For alumina, the grain sizes are higher in the surface than in the volume in the presence of SiC for the four samples. It is the opposite situation in the absence of SiC for A-0Z, A-3YZ and A-8YZ. The alumina grain sizes in the surface decrease from the SiC to the noSiC configuration for A-0Z, A-3YZ and A-10CeZ but not for A-8YZ. The average grain sizes of zirconia are closer from each other. There is only a significant difference for A-3YZ, for which the grain size increases from the SiC to the noSiC configuration.

### 3.3. Phase composition

The XRD patterns of the sintered samples are presented in Figure 4. The XRD patterns all show peaks associated with α-alumina (JCPDS file: 01-089-7717). Both A-0Z samples contain a mixture of tetragonal (JCPDS file: 04-013-6649) and monoclinic (JCPDS file: 00-065-0687) zirconia phases. The A-3YZ and A-8YZ samples have only one zirconia phase, tetragonal and cubic (JCPDS file: 01-084-4048) respectively. The A-10CeZ sample sintered with SiC has a mixture of tetragonal and monoclinic phase whereas the one sintered without SiC contains mainly tetragonal phase.

### 3.4. Heating of pellets in MW single-mode cavity

Figure 5 shows the evolution of temperature *vs* time curves for the four samples submitted to a constant incident power in the MW single-mode cavity. The curves of monolithic alumina was added for comparison. The four samples started to heat during the first minute and reached close values of temperature after one minute: 160°C, 177°C, 191°C and 167°C for A-0Z, A-3YZ, A-8YZ and A-10CeZ, respectively. After one minute, the samples behaved differently. The A-0Z and A-10CeZ pellets reached a plateau at around 165°C in few seconds. This

behaviour is similar to the one of monolithic alumina. The temperature of A-3YZ slowly increased and reached 300°C after 10 minutes. Finally, A-8YZ heated with a higher rate than A-3YZ (410°C after 8 minutes *vs* 292°C for A-3YZ). After 8 minutes, a thermal runaway was observed. A temperature of 800°C was achieved in one minute. The MW power was then turned off to avoid damaging the cavity.

## 4. Discussion

The characterizations show that the four sintered samples are highly dense with fine microstructures (submicronic grains in the two phases).

Comparison between sintering with or without SiC for one given sample reveals some differences.

The final densities were higher when SiC was used for A-0Z, A-3YZ and A-10CeZ, highlighting the well-known positive role of MW absorbent SiC. This was not the case for A-8YZ, for which the final density was higher without SiC. Similar trends were observed for microstructures. The average grain sizes of alumina were higher in the surface than in the volume in the presence of SiC. When the SiC ring was removed, the average grain sizes of alumina decreased in the surface, except for A-8YZ. The average grain sizes of zirconia were more homogeneous for all the samples and the two configurations. Therefore, alumina was more affected by the presence or absence of SiC than zirconia. Due to their respective dielectric properties, alumina is more probably heated by radiative heating by SiC and zirconia is more prone to a direct heating by MW. But the particular case of A-8YZ (which was denser for noSiC sintering) shows that 8YZ had a beneficial effect on the sintering behaviour of the composite. In a previous article [34], an "internal susceptor" effect of 3YZ in a ZTA composite was observed and discussed for ZTA with different volume fractions of zirconia. It can be hypothesized that zirconia grains preferentially heat by interaction with MW and then heat

11

surrounding alumina grains by conduction. Here, the differences between A-8YZ and the other samples (*i.e.*, higher density for A-8YZ without SiC and opposite case for the three other samples) show that this "internal susceptor" effect depends on the type of zirconia introduced in the composite. Moreover, A-8YZ underwent a thermal runaway when it was heated in the single-mode cavity (see Figure 5). Therefore, a local heating of 8YZ grains in A-8YZ can be hypothesized, which can explain the higher final density of A-8YZ without SiC. This local heating is probably more important for A-8YZ, in comparison with the three other samples.

For the densification curves, shifts of the curves in the initial and intermediate stages of sintering were observed between SiC and noSiC configurations for one given sample. A shift of the curve towards lower (resp. higher) temperature for noSiC sintering can be related to an easier (resp. more difficult) heating and thus, to an easier densification of the sample. Three cases can be distinguished. A-0Z and A-10CeZ were the most difficult to densify in the intermediate stage in the noSiC configuration because they exhibited the highest shifts of the curves towards higher temperatures (*i.e.*, high values of $\Delta T_{noSiC-SiC}$). A-3YZ was also quite difficult to densify without SiC but the value of $\Delta T_{noSiC-SiC}$ was lower than for A-0Z and A-10CeZ. A-8YZ sample had a different behaviour because its densification curve without SiC was shifted towards lower temperature (negative value of $\Delta T_{noSiC-SiC}$). These observations are consistent with the results for the final densities.

The experiments of heating in single-mode cavity point out the same three situations. A-0Z and A-10CeZ had a similar behaviour and reached the lowest temperatures. A-3YZ was able to heat better than A-0Z and A-10CeZ. Finally, A-8YZ was the easiest sample to heat and even underwent a delayed thermal runaway. The addition of 0Z and 10CeZ to alumina matrix did not bring any improvement to MW coupling, compared with monolithic alumina (see Figure 5). The mixture of 3YZ and alumina helped to obtain an intermediate behaviour between alumina and zirconia and suppressed the thermal runaway undergone by 3YZ (submitted to the

same experimental procedure in [34]). Mixing 8YZ with alumina did not prevent from the thermal runaway. But this thermal runaway is probably responsible for a local heating of zirconia grains in the composite, which facilitates MW heating without SiC.

These differences of behaviour under MW can be linked to the chemical composition of zirconia and the generated point defects. In A-0Z, the 0Z powder does not contain any dopant and in A-10CeZ, the 10CeZ one is stabilized with the tetravalent cation $Ce^{4+}$ (same valence as $Zr^{4+}$). Thus, A-10CeZ and A-0Z do not have any excess of point defects due to the presence of a stabilizing oxide. On the contrary, 3YZ and 8YZ are stabilized by introduction of the trivalent $Y^{3+}$ cation in the lattice. This trivalent dopant generates an excess of oxygen vacancies in the lattice for charge compensation [10]. The reaction relative to the creation of point defects can be expressed with the Kröger-Vink notation:

$$Y_2O_3 \rightarrow 2Y'_{Zr} + V_O^{\bullet\bullet} + 3O_O^X \quad \text{(Eq 5)}$$

These point defects are associated to the creation of dopant-vacancy dipoles. Under the action of a high-frequency electric field, the dipole moment tends to align in the direction of the electric field [35, 36]. Dissipation under thermal energy occurs by internal friction of the oscillating dipoles.

Moreover, the difference of behaviour between A-3YZ and A-8YZ can be related to the difference of concentration of $Y^{3+}$, and thus of concentration of point defects in the lattice. Nightingale *et al.* [37] studied MW sintering of 3YZ and 8YZ and obtained higher densities for 8YZ samples (compared with 3YZ). But 3YZ and 8YZ also have different crystalline structures, which can also have an influence. Thompson *et al.* measured dielectric properties of different doped zirconia samples at room temperature [22] and concluded about a high influence of their crystalline structures. The four samples studied here have different phase compositions after sintering. A-3YZ and A-8YZ had the same zirconia phases after SiC and noSiC sintering: tetragonal and cubic zirconia, respectively. In both cases, the high temperature phases were

13

stabilized after sintering due to $Y_2O_3$ doping. Both A-0Z have tetragonal and monoclinic zirconia phases (the volume fraction of monoclinic phase was 70 % for A-0Z sintered with SiC and 74 % for A-0Z sintered without SiC). These values are close to the ones obtained by Biotteau-Deheuvels *et al.* [38] for ZTA containing 25 vol% unstabilized zirconia with grain sizes around 0.3-0.34 µm. The retention of tetragonal zirconia in unstabilized zirconia after sintering is due to compression stresses brought by the stiff alumina matrix. The case of A-10CeZ is slightly more complex. The sample sintered with SiC contains tetragonal and monoclinic phase (75 vol%) whereas the one sintered without SiC has only tetragonal phase. This difference can be explained by a difference of heating mode. In a previous study, Fornabaio *et al.* [39] calcined 10CeZ powder at different temperatures and observed an influence of the calcination temperature on the phase composition. The volume fraction of monoclinic phase decreased with increasing calcination temperature until 1150°C and then increased at 1450°C. Based on these results, it can be hypothesized here that the two A-10CeZ samples did not reach the same temperatures. The sample sintered with SiC probably reached a higher temperature due to radiative heating by SiC, which led to a higher monoclinic content. On the contrary, the sample sintered without SiC was probably less hot, due to the low coupling of 10CeZ with MW. The link between behaviour under MW and crystalline structures is difficult to establish with our results because each sample has a different phase composition. Deeper investigations would be necessary with thermal treatments at lower temperatures to follow the evolution of phase composition with temperatures.

In this study, heating in single-mode cavity and sintering experiments show important differences of behaviour of ZTA materials according to the type of zirconia added to the alumina matrix. In particular, the type and amount of dopants in zirconia can notably change the behaviour. The difference of behaviour between ZTA with 3 or 8 mol% yttria-stabilized zirconia highlights this point. It points out the importance of a deep understanding of the

MW/materials interaction and relating it to the characteristics of the material in order to optimize MW sintering (*i.e.*, choice of the most relevant materials to heat under MW, choice of thermal treatments, design of sintering cells).

## 5. Conclusion

In this study, four different ZTA samples (alumina and 20 vol% of unstabilized, 3 mol% yttria-stabilized, 8 mol% yttria-stabilized and 10 mol% ceria-stabilized zirconia) were sintered in a MW multimode cavity with two different sintering cells (with and without SiC) and then characterized. The values of final densities, the densification curves and the experiments in the single-mode cavity showed different behaviours, which can be related to the composition of the samples. Three situations can be distinguished:

- the ZTA containing the unstabilized zirconia and the ceria-doped zirconia had the lowest heating ability in the single-mode cavity and were densified with difficulties without SiC. It can be related to the absence of excess of $O^{2-}$ vacancies in the crystalline lattice of zirconia.

- the ZTA containing 3 mol% yttria-doped zirconia was less difficult to heat and was densified without SiC with less difficulty than the previous ones, the mixture between alumina and 3YZ led to a heating without thermal runaway;

- the ZTA containing 8 mol% yttria-doped zirconia heated easily under MW and was densified better without SiC, the mixture between alumina and 8YZ underwent a thermal runaway.

The two latter cases can be related to the excess of $O^{2-}$ vacancies generated in the crystalline lattice by doping with $Y^{3+}$. The excess of dipoles in the lattice can explain the high coupling ability of the sample. However, the final phase composition of the samples did not allow

15

concluding about the influence of the crystalline structure of zirconia on the MW/material interactions.

Addition of zirconia to an alumina matrix has a positive effect on the MW/material interactions but it highly depends on the type of zirconia. The results highlight the importance of a careful understanding of the MW/materials interaction to optimize MW sintering. It is particularly important in view of the use of MW sintering at an industrial scale.

Beyond these results, deeper investigation could be carried out, especially to investigate deeper the influence of the crystalline structure and the phase stability of zirconia during MW sintering.

**References**

[1] A.C.O. Lopes, Microstructural, mechanical, and optical characterization of an experimental aging-resistant zirconia-toughened alumina (ZTA) composite, Dent. Mater. 36 (2020) 365-374. https://doi.org/10.1016/j.dental.2020.08.010

[2] J. Chevalier, L. Gremillard, Zirconia as a biomaterial, Compr. Biomater. 1 (2011) 95-108. https://doi.org/10.1016/B978-0-08-055294-1.00017-9

[3] B.K. Singh, K. Ghosh, S.S. Roy, B. Mondal, N. Mandal, Correlation between microstructure and mechanical properties of $YSZ/Al_2O_3$ ceramics and its effect on high speed machining of steel, Trans. Ind. Ceram. Soc. 77 (2018) 1-7. https://doi.org/10.1080/0371750X.2018.1528889

[4] J. Chevalier, L. Gremillard, Ceramics for medical applications: A picture for the next 20 years, J. Eur. Ceram. Soc. 29 (2009) 1245-1255. https://doi.org/10.1016/j.jeurceramsoc.2008.08.025

[5] A.H. De Aza, J. Chevalier, G. Fantozzi, M. Schehl, R. Torrecillas, Crack growth resistance of alumina, zirconia and zirconia toughened alumina ceramics for joint prostheses, Biomaterials 23 (2002) 937-945. https://doi.org/10.1016/S0142-9612(01)00206-X

[6] O.Y. Zadorozhnaya, T.A. Khabas, O.V. Tiunova, S.E. Malykhin, Effect of grain size and amount of zirconia on the physical and mechanical properties and the wear resistance of zirconia-toughened alumina, Ceram. Int. 46 (2020) 9263-9270. https://doi.org/10.1016/j.ceramint.2019.12.180

[7] J. Chevalier, P. Taddei, L. Gremillard, S. Deville, G. Fantozzi, J.F. Bartolomé, C. Pecharroman, J.S. Moya, L.A. Diaz, R. Torrecillas, S. Affatato, Reliability assessment in advanced nanocomposite materials for orthopaedic applications, J. Mech. Behav. Biomed. Mater. 4 (2011) 303-314. https://doi.org/10.1016/j.jmbbm.2010.10.010

[8] J.R. Kelly, I. Denry, Stabilized zirconia as a structural ceramic: An overview, Dent. Mater. 24 (2008) 289-298. https://doi.org/10.1016/j.dental.2007.05.005

[9] J.Chevalier, A. Liens, H. Reveron, F. Zhang, P. Reynaud, T. Douillard, L. Preiss, V. Sergo, V. Lughi, M. Swain, N. Courtois, Forty years after the promise of «ceramic steel?»: Zirconia-based composites with a metal-like mechanical behavior, J. Am. Ceram. Soc. 103 (2020) 1482–1513. https://doi.org/10.1111/jace.16903

[10] P. Li, I.-W. Chen, J.E. Penner-Hahn, Effect of dopants on zirconia stabilization - An X-ray absorption study: I, trivalent dopants, J. Am. Ceram. Soc. 77 (1994) 118-128. https://doi.org/10.1111/j.1151-2916.1994.tb06964.x

[11] M.E. Roy, L.A. Whiteside, B.J. Katerberg, J.A. Steiger, Phase transformation, roughness, and microhardness of artificially aged yttria- and magnesia-stabilized zirconia femoral heads, J. Biomed. Mater. Res. A. 83A (2007) 1096-1102. https://doi.org/10.1002/jbm.a.31438

[12] S.Y. Kwon, I.-H. Jung, Critical evaluation and thermodynamic optimization of the CaO-ZrO$_2$ and SiO$_2$-ZrO$_2$ systems, J. Eur. Ceram. Soc. 37 (2017) 1105-1116. https://doi.org/10.1016/j.jeurceramsoc.2016.10.008

[13] M. Yoshimura, T. Noma, K. Kawabata, S. Sōmiya, Role of H$_2$O on the degradation process of Y-TZP, J. Mater. Sci. Lett. 6 (1987) 465-467. https://doi.org/10.1007/BF01756800

[14] V. Nečina, W. Pabst, Influence of the heating rate on grain size of alumina ceramics prepared via spark plasma sintering (SPS), J. Eur. Ceram. Soc. 40 (2020) 3656-3662. https://doi.org/10.1016/j.jeurceramsoc.2020.03.057

[15] B. Suleiman, H. Zhang, Y. Ding, Y. Li, Microstructure and mechanical properties of cold sintered porous alumina ceramics, Ceram. Inter. 48 (2022) 13531-13540. https://doi.org/10.1016/j.ceramint.2022.01.232

[16] J.-M. Chaix, Microwave sintering of ceramics, in: M. Pomeroy (Ed.), Encyclopedia of Materials: Technical Ceramics and Glasses, Elsevier, Oxford, 2021: pp. 327-341. https://doi.org/10.1016/B978-0-12-818542-1.00004-7

[17] R.R. Mishra, A.K. Sharma, Microwave-material interaction phenomena: Heating mechanisms, challenges and opportunities in material processing, Compos. Part Appl. Sci. Manuf. 81 (2016) 78-97. https://doi.org/10.1016/j.compositesa.2015.10.035

[18] J. Batt, W.H. Sutton, J.G.P. Binner, T.E. Cross, A parallel measurement programme in high temperature dielectric property measurements: an update, Ceramic Transactions: Microwaves - theory and application in materials processing III 59 (1995) 243-250.

[19] M. Arai, J.G.P. Binner, T.E. Cross, Comparison of techniques for measuring high-temperature microwave complex permittivity: measurements on an alumina/zirconia system, J. Microw. Power Electromagn. Energy 31 (1) (1996) 12-18. https://doi.org/10.1080/08327823.1996.11688287

[20] M. Bhattacharya, T. Basak, A review on the susceptor assisted microwave processing of materials, Energy 97 (2016) 306-338. http://dx.doi.org/10.1016/j.energy.2015.11.034

[21] C. Manière, T. Zahrah, E.A. Olevsky, Inherent heating instability of direct microwave sintering process: Sample analysis for porous 3Y-ZrO$_2$, Scripta Mater. 128 (2017) 49-52. http://dx.doi.org/10.1016/j.scriptamat.2016.10.008

[22] D.P. Thompson, A.M. Dickins, J.S. Thorp, The dielectric properties of zirconia, J. Mater. Sci. 27 (1992) 2267-2271. https://doi.org/10.1007/BF01117947

[23] R.R. Menezes, R.H.G.A. Kiminami, Microwave sintering of alumina–zirconia nanocomposites, J. Mater. Process. Technol. 203 (2008) 513-517. https://doi.org/10.1016/j.jmatprotec.2007.10.057

[24] R. Benavente, M.D. Salvador, F.L. Penaranda-Foix, E. Pallone, A. Borrell, Mechanical properties and microstructural evolution of aluminA-0Zirconia nanocomposites by microwave sintering, Ceram. Int. 40 (2014) 11291-11297. https://doi.org/10.1016/j.ceramint.2014.03.153

[25] R. Vasudevan, T. Karthik, S. Ganesan, R. Jayavel, Effect of microwave sintering on the structural and densification behavior of sol-gel derived zirconia toughened alumina (ZTA) nanocomposites, Ceram. Int. 39 (2013) 3195-3204.
https://doi.org/10.1016/j.ceramint.2012.10.004

[26] M.W. Khalid, Y.I. Kim, M.A. Haq, D. Lee, B.S. Kim, B. Lee, Microwave hybrid sintering of Al$_2$O$_3$ and Al$_2$O$_3$-ZrO$_2$ composites, and effects of ZrO$_2$ crystal structure on mechanical properties, thermal properties, and sintering kinetics, Ceram. Int. 46 (2020) 9002-9010. https://doi.org/10.1016/j.ceramint.2019.12.147

[27] D. Zymelka, S. Saunier, J. Molimard, D. Goeuriot, Contactless monitoring of shrinkage and temperature distribution during hybrid microwave sintering, Adv. Eng. Mater. 13 (2011) 901-905. https://doi.org/10.1002/adem.201000354

[28] F. Zuo, C. Carry, S. Saunier, S. Marinel, D. Goeuriot, Comparison of the microwave and conventional sintering of alumina: Effect of MgO doping and particle size, J. Am. Ceram. Soc. 96 (2013) 1732-1737. https://doi.org/10.1111/jace.12320

[29] C. Meunier, F. Zuo, N. Peillon, S. Saunier, S. Marinel, D. Goeuriot, In situ study on microwave sintering of ZTA ceramic: Effect of $ZrO_2$ content on densification, hardness, and toughness, J. Am. Ceram. Soc. 100 (2017) 929-936. https://doi.org/10.1111/jace.14658

[30] M.I. Mendelson, Average grain size in polycrystalline ceramics, J. Am. Ceram. Soc. 52 (1969) 443-446. https://doi.org/10.1111/j.1151-2916.1969.tb11975.x

[31] R.C. Garvie, P.S. Nicholson, Phase analysis in zirconia systems, J. Am. Ceram. Soc. 55 (1972) 303-305. https://doi.org/10.1111/j.1151-2916.1972.tb11290.x

[32] H. Toraya, M. Yoshimura, S. Somiya, Calibration curve for quantitative analysis of the monoclinic-tetragonal $ZrO_2$ system by X-ray diffraction. J. Am. Ceram. Soc. 67 (1984) 119-121. https://doi.org/10.1111/j.1151-2916.1984.tb19715.x

[33] I. Ghorbel, P. Ganster, N. Moulin, C. Meunier, J. Bruchon, Experimental and numerical thermal analysis for direct microwave heating of silicon carbide, J. Amer. Ceram. Soc. 104 (2021) 302-312. https://doi.org/10.1111/jace.17451

[34] N. Khalile, C. Petit, C. Meunier, F. Valdivieso, Hybrid microwave sintering of Zirconia Toughened Alumina in a multimode cavity - Influence of the content of 3 mol% yttria stabilized zirconia and sintering configurations, Open Ceram. 14 (2023) 100371. https://doi.org/10.1016/j.oceram.2023.100371

[35] A. Lakki, R. Herzog, M. Weller, H. Schubert, C. Reetz, O. Görke, M. Kilo, G. Borchardt, Mechanical loss, creep, diffusion and ionic conductivity of $ZrO_2$-8 mol%$Y_2O_3$ polycrystals, J. Eur. Ceram. Soc. 20 (2000) 285-296. https://doi.org/10.1016/S0955-2219(99)00162-4

[36] M. Weller, R. Herzog, M. Kilo, G. Borchardt, S. Weber, S. Scherrer, Oxygen mobility in yttria-doped zirconia studied by internal friction, electrical conductivity and tracer diffusion experiments, Sol. Stat. Ion. 175 (2004) 409-413. https://doi.org/10.1016/j.ssi.2003.12.044

[37] S.A. Nightingale, H.K. Worner, D.P. Dunne, Microstructural development during the microwave sintering of yttria-zirconia ceramics, J. Am. Ceram. Soc. 80 (1997) 394-400. https://doi.org/10.1111/j.1151-2916.1997.tb02843.x

[38] K. Biotteau-Deheuvels, L. Zych, L. Gremillard, J. Chevalier, Effects of Ca-, Mg- and Si-doping on microstructures of alumina-zirconia composites, J. Eur. Ceram. Soc. 32 (2012) 2711-2721. https://doi.org/10.1016/j.jeurceramsoc.2011.11.011

[39] M. Fornabaio, P. Palmero, R. Traverso, C. Esnouf, H. Reveron, J. Chevalier, L. Montanaro, Zirconia-based composites for biomedical applications: Role of second phases on composition, microstructure and zirconia transformability, J. Eur. Ceram. Soc. 35 (2015) 4039-4049. http://dx.doi.org/10.1016/j.jeurceramsoc.2015.04.027

**Figures' and tables' captions:**

Figure 1: Densification curves for the four samples for MW sintering (a) with and (b) without SiC

Figure 2: SEM images of the A-3YZ samples sintered with SiC taken at different magnifications: (a) x 5000 and (b) x 20000

Figure 3: Alumina (noted A) and zirconia (noted Z) average grain sizes (and standard deviations) for the four samples sintered in MW sintering (a) with and (b) without SiC

Figure 4: XRD patterns of the samples sintered (a) with and (b) without SiC

Figure 5: Temperature *vs* time for the four samples heated in a single-mode cavity

Supplementary figure 1: SEM images of the (a) A-0Z, (b) A-8YZ and (c) A-10CeZ samples sintered with SiC taken at magnification x 20000

Table 1: Values of final relative densities for the sintered samples

Table 2: Temperatures for which a relative density of 65 % is reached for the four samples and the two sintering configurations and differences between these temperatures

Table 1:

| Samples | Sintering configurations | Relative density (% T.D.) |
|---------|--------------------------|---------------------------|
| A-0Z | SiC | 97.2±0.6 |
| | noSiC | 97.0±0.6 |
| A-3YZ | SiC | 97.7±0.5 |
| | noSiC | 97.0±0.1 |
| A-8YZ | SiC | 95.0±0.1 |
| | noSiC | 97.0±0.4 |
| A-10CeZ | SiC | 99.1±0.1 |
| | noSiC | 97.1±0.2 |

Table 1:

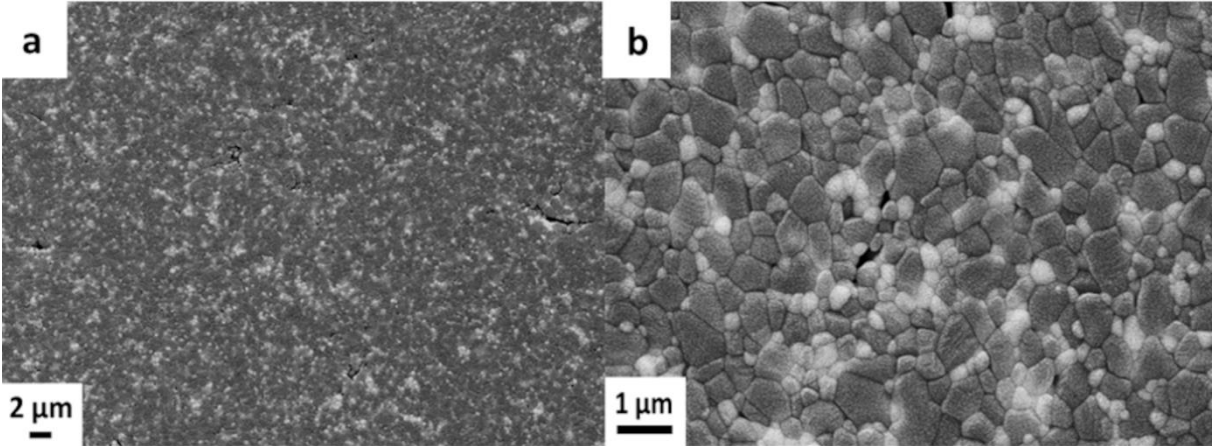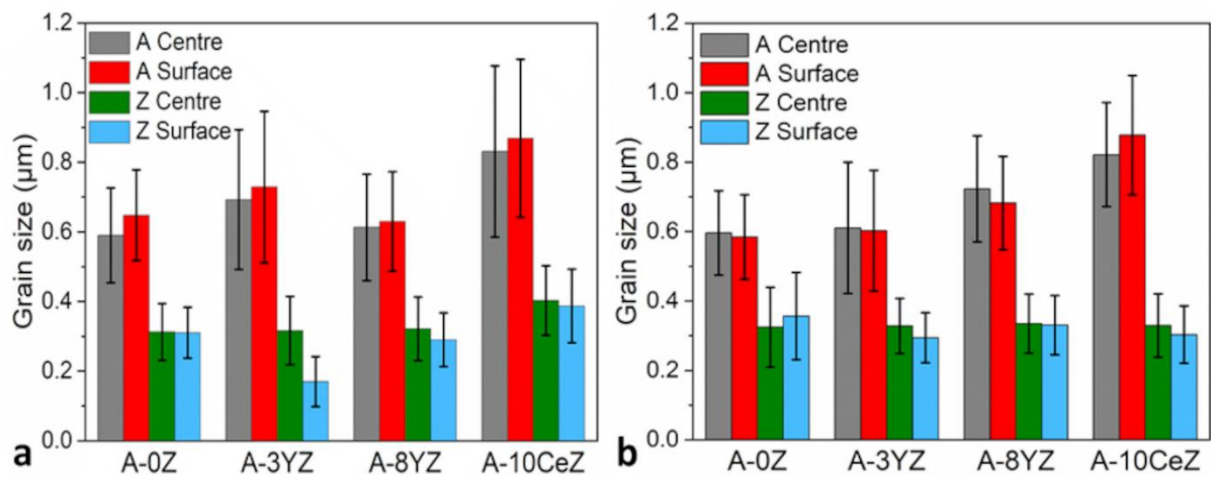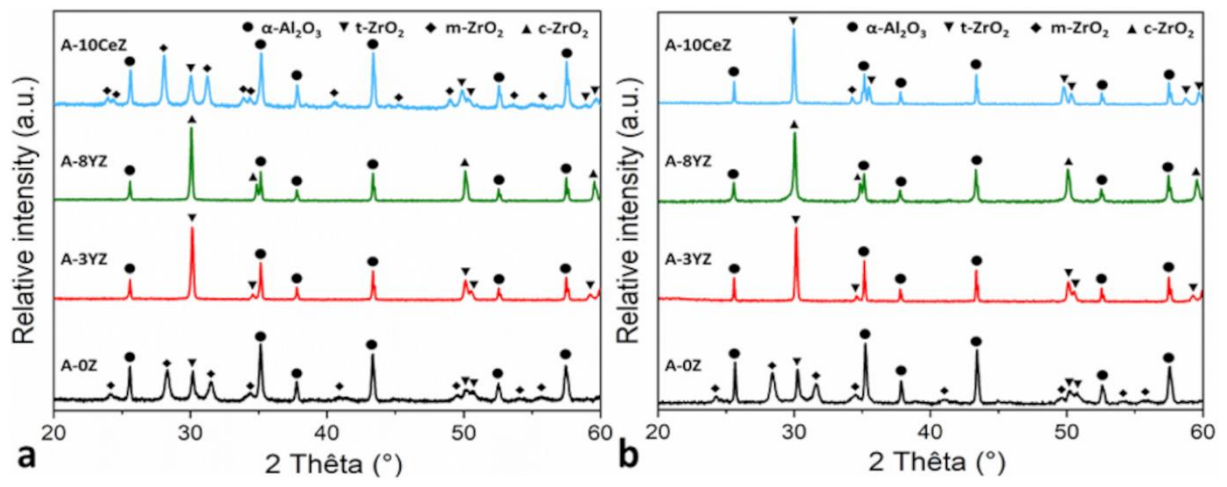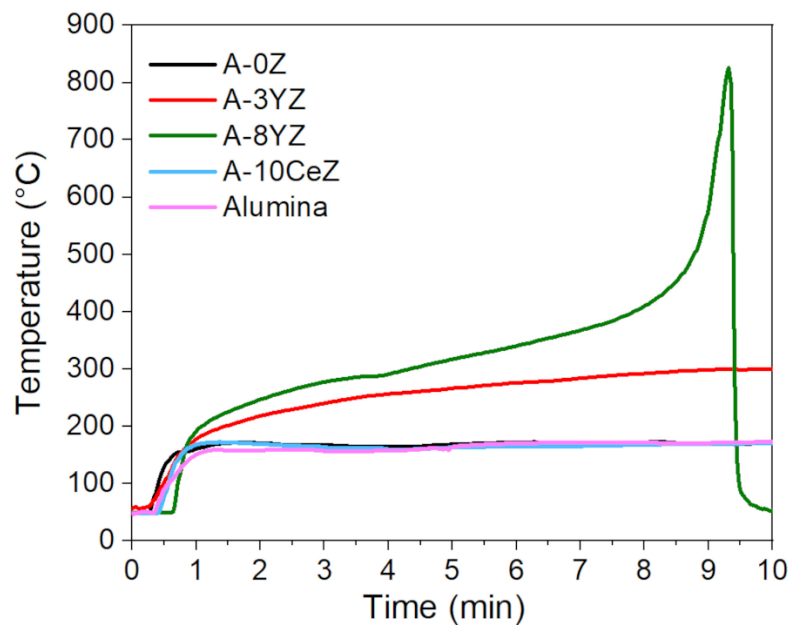| Samples | $T_{SiC}$ | $T_{noSiC}$ | $\Delta T_{noSiC - SiC} = T_{noSiC} - T_{SiC}$ |
|---------|-----------|-------------|------------------------------------------------|
| A-0Z | 1471 | 1550 | 79 |
| A-3YZ | 1405 | 1455 | 40 |
| A-8YZ | 1512 | 1495 | -17 |
| A-10CeZ | 1405 | 1475 | 70 |

Figure 1:
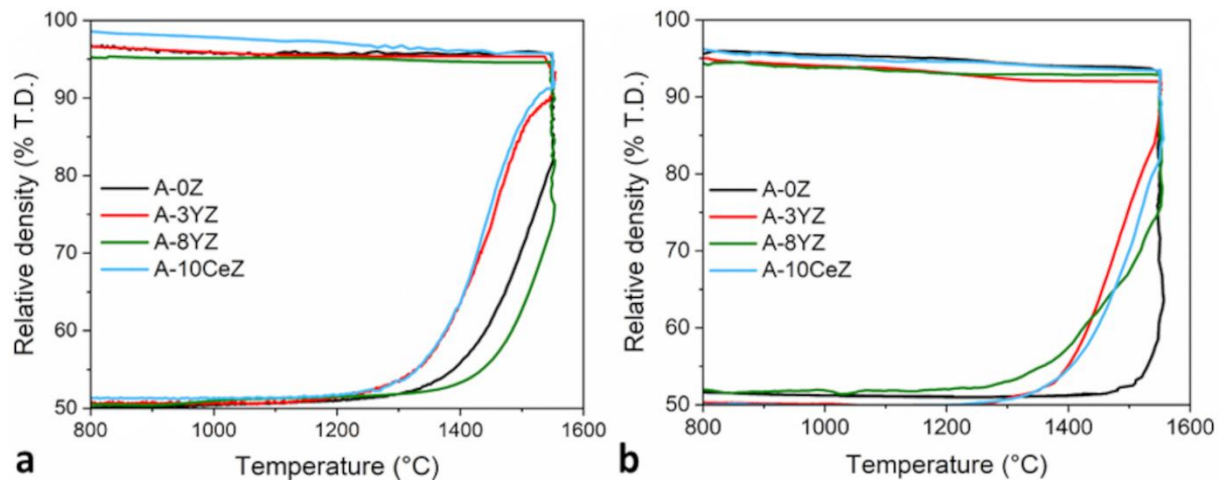
Figure 2:

Figure 3:

Figure 4:

Figure 5:

Supplementary figure 1 :